Journal of Crystal Growth 337 (2011) 52–59

Contents lists available at SciVerse ScienceDirect

Journal of Crystal Growth

journal homepage: www.elsevier.com/locate/jcrysgro

Microstructure evolution of directionally solidified Ti–46Al–0.5W–0.5Si alloy

Jianglei Fan, Xinzhong Li*, Yanqing Su, Ruirun Chen, Jingjie Guo, Hengzhi Fu

School of Material Science and Engineering, Harbin Institute of Technology, Harbin 150001, PR China

ARTICLE INFO

Article history:
Received 14 August 2010
Received in revised form
21 September 2011
Accepted 28 September 2011
Communicated by M. Rettenmayr
Available online 12 October 2011

Keywords:
A1. Directional solidification
A1. Dendrites
A2. Bridgman technique
B1. Alloys

ABSTRACT

Directional solidification experiments were performed on the intermetallic Ti–46Al–0.5W–0.5Si (at%) alloy using a Bridgman-type furnace. The effect of growth rate on the solidification behavior and microstructure parameters was determined. After directional solidification, the microstructure is composed of α_2/γ lamellar structures and fine Ti_5Si_3 precipitates. During the solidification process, W segregates into dendritic cores of α phase, and Si segregates into interdendritic regions. The enrichment of Si leads to the formation of Ti_5Si_3 phases. The primary dendritic arm spacings and interlamellar spacings decrease with the increasing growth rate. Because of the change of preferred growth direction (PGD), the lamellar orientation is not perpendicular to the growth direction, even if the α phase is the primary phase. The variation of lamellar orientation can be attributed to two factors. One is the history-dependence on the lamellar orientation of unmelted as-cast crystals near the initial interface of directional solidification. The other is the variation of PGD of the α phase. With the increasing growth rate, the variation of PGD of α phase is as follows: $\langle 0001\rangle \rightarrow \langle 10\bar{1}1\rangle \rightarrow \langle \bar{2}\bar{2}43\rangle \rightarrow \langle 10\bar{1}1\rangle$.

1. Introduction

Intermetallic γ-TiAl based alloys have been considered as a new generation of high temperature structural material for aerospace and automotive industries due to their low-density, good oxidation resistance and high temperature strength [1–4]. Of the many microstructures that can be formed in TiAl-based alloys, the fully lamellar microstructure consisting of γ-phase (TiAl) and α_2-phase (Ti_3Al) displays a good combination of room temperature toughness and elevated temperature strength [5]. However, initial application of TiAl alloys is limited to major obstacles such as low room-temperature ductility, the difficulty in processing then to fabricate a component and poor oxidation resistance above 800 °C [1–4,6]. Recent researches show that TiAl-based alloys with aligned lamellar orientation have a good combination of strength and ductility in a wide range of temperature [5,7–10]. Because the lamellar structure is not formed from the liquid but by the solid-state transformation [5,7–10], the orientation of the high temperature α phase must be initially controlled to obtain the preferred lamellar orientation [8–11]. Furthermore, the aligned lamellar structure can be obtained by directional solidification and seeding technique with a seed having specific α orientation [7,9,11–15].

Presently, many efforts are concentrated on TiAl-based alloys with various alloying elements [8,9,16–21], such as W, Ta, Nb or Si, which are added to improve the high temperature resistance, lamellar structure stability or oxidation resistance. However, such alloying elements can lead to a complex multiphase material and affect the solidification behavior and solid-state transformation. These changes can affect subsequent heat treatment and result in different mechanical properties [22]. Therefore, for multi-component TiAl alloys, to understand the solidification pathway, microsegregation and microstructure variation are interesting to further progress in commercial applications.

Directional solidification is an appropriate technique to research solidification behavior of alloy under defined solidification conditions [23]. Previous studies [8,12,24] on directional solidification experiments of TiAl-based alloys have focused on controlling lamellar orientation by seeding technique or changing the solidification path. However, there is a lack of information about solidification behavior of these multiphase TiAl-based alloys.

Therefore, the purpose of this work is to study the solidification behavior, microstructure evolution and chemical heterogeneity of Ti–46Al–0.5W–0.5Si (at%) alloy by directional solidification technique. The variation of lamellar orientation after directional solidification is also discussed. These results will contribute to increase the understanding of the solidification behavior and lamellar orientation control of multi-component TiAl-based alloys.

2. Experiments

Master ingot with nominal composition of Ti–46Al–0.5W–0.5Si (at%) was prepared using Ti (99.96%), Al (99.99%), W (99.98%) and Si (99.96%) of commercial purity in a cold crucible induction furnace under an argon atmosphere. The chemical composition of the alloy is shown in Table 1, which was measured by spectral analysis. The ingot was machined to rods with 3 mm

* Corresponding author. Tel.: +86 451 86418815; fax: +86 451 86415776.
E-mail addresses: JLFan2011@163.com (J. Fan), hitlxz@126.com (X. Li).

0022-0248/$ - see front matter © 2011 Elsevier B.V. All rights reserved.
doi:10.1016/j.jcrysgro.2011.09.053

in diameter and 100 mm in length by spark machining. The fine diameter of specimens was chosen to achieve a high temperature gradient during directional solidification. The experiments were performed in a Bridgman-type furnace, as previously described in Ref. [25]. Each specimen was placed into 99.99 pct pure alumina crucible of 4/5.5 mm diameter (inside/outside diameter) and length of 120 mm. After heating for 4 h to 1773 K and 30 min temperature stabilization, the specimen was pulled at a selected rate (growth rates ranged from 1 μm/s to 100 μm/s). After growing about 35 mm, the sample was quenched into the Ga–In–Sn alloy to preserve the solid/liquid interface.

The temperature gradient was measured by W/Re thermocouples that were placed near the outside surface of the alumina tube. One thermocouple was placed about 5 mm from the bottom of the sample, which was near the solid–liquid interface. Other was placed 15 mm from the bottom of the sample where the liquid region was. The measured temperature gradient close to the solid/liquid interface was 20 K/mm.

The phases were identified by a Rigaku D/max-RB X-ray diffractometer with monochromatic Cu-Kα radiation. Both optical microscopy (OM) and scanning electron microscopy (SEM) were used to characterize the microstructure of the samples after polishing and etching by a solution of 10 ml HF–10 ml HON_3–180 ml H_2O. Backscattered electron imagining (BSE) was used to identify the phases present. In addition, energy-dispersive spectrometry (EDS) was used to analyze the composition of each phase.

The primary dendritic (or cellular) spacing was measured from transverse sections of specimens with a triangle method [26,27]. The interlamellar spacing was measured from BSE images with a linear intercept method [28]. The value of interlamellar spacing is the thickness of one α and γ lamella nearby.

Table 1
Chemical composition of the Ti–46Al–0.5W–0.5Si (at%) alloy.

Element	Ti	Al	W	Si	O	Other
at%	Balance	45.27	0.62	0.52	0.05	< 0.1

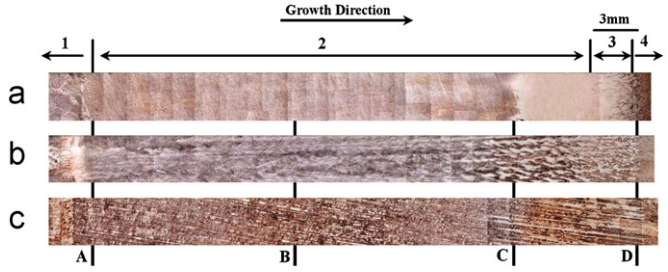

Fig. 1. Macrostructures of longitudinal section of directionally solidification specimens at growth rates of 3 μm/s (a), 10 μm/s (b) and 70 μm/s (c). The numbers show the different regions—1: unmelted region, 2: directional solidification region, 3: mushy zone, 4: quenched zone.

3. Results and discussion

3.1. Macrostructure

The macrostructures of directionally solidified (DS) specimens at different growth rates are shown in Fig. 1. There are four distinguished sections in the DS specimens, which are unmelted region, directional solidification region, mushy zone and quenched zone. It should be noted that the length of each region is different from each other due to different solidification conditions for different specimens. In unmelted-region, the temperature is not high enough to melt the original alloy. The equiaxed grains coarsened by heat treatments are caused by heat conducting from the high temperature zone. Up towards this region, the original alloy is completely melted. The number of columnar grains in DS region depends on the growth rate and position in the specimen, and increases with the increasing growth rate and decreases with the increasing distance from the bottom of the specimen. These columnar grains are well aligned along the growth direction, and the size of columnar grains decreases with the increase of growth rate. Fig. 2 shows the microstructures corresponding to DS

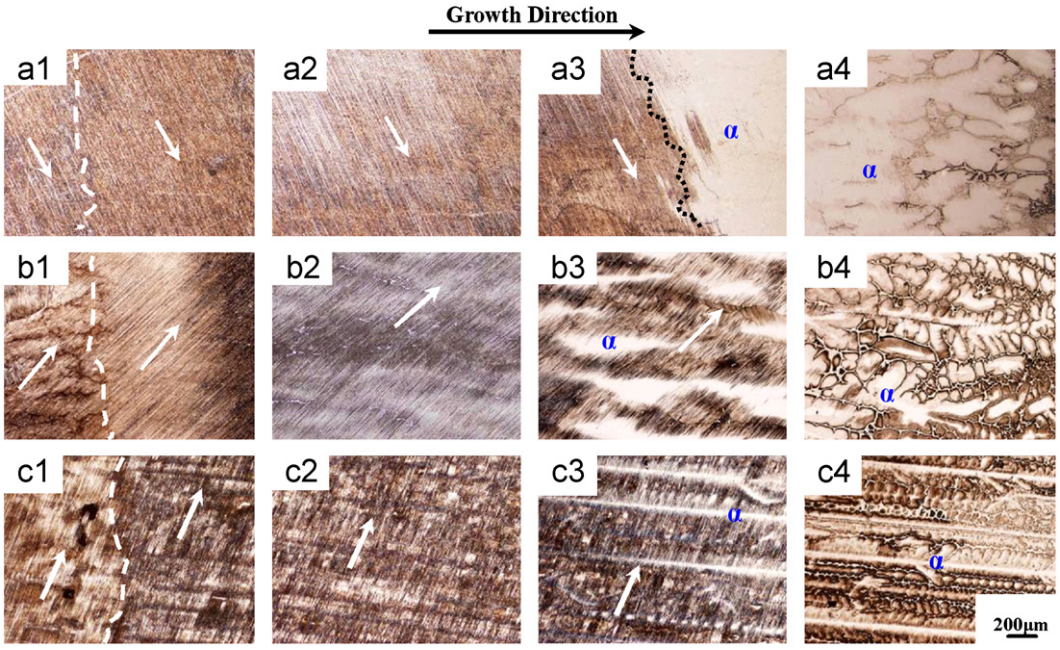

Fig. 2. Microstructures of directionally solidified specimens at growth rates of 3 μm/s (a), 10 μm/s (b) and 70 μm/s (c). Parts 1–4 in different specimens correspond to the regions A, B, C and D in Fig. 1, respectively. The white broken lines in a1, b1 and c1 indicate the initial interface of directional solidification. The black dot line in a3 shows the solid–state transition interface. The arrows indicate the orientations of lamellar structures.

specimens in Fig. 1. Parts 1–4 for different specimens correspond to regions A, B, C and D in Fig. 1, respectively. The initial interface of directional solidification separates the unmelted region and directional solidification region (Fig. 2a1, b1 and c1). The initial interface is the beginning position of directional solidification, which can influence the lamellar structure of DS specimens.

3.2. Microstructure

3.2.1. Phases formation

From the XRD diffraction pattern (Fig. 3), the DS microstructure is composed of γ-TiAl, α_2-Ti_3Al and Ti_5Si_3 phases. Fig. 4 shows the typical microstructure in transverse sections of DS specimens. Ti_5Si_3 phases distribute in interdendritic regions (Fig. 4a). The compositions analyzed by EDS for points labeled in Fig. 4a are listed in Table 2. According to the EDS results, the black phase is the γ phase and the gray one is the α_2 phase while the white is the Ti_5Si_3 phase. In addition, some black particles can be found in the specimens (Fig. 4a). The chemical composition of these particles determined by EDS is 46.70 at% Al, 52.20 at% O, 1.02 at% Ti and 0.08 at% Si. It indicates that these particles are Al_2O_3. These Al_2O_3 particles are formed during solidification because of the reaction between the crucible and melt.

The type of primary phase in TiAl alloys can be identified by the symmetry of dendritic shape [33], i.e. the angle between the secondary dendritic arm and the primary dendritic spine. For the present alloy, the dendrites have a shape with a six-fold symmetry, according to the morphologies of the dendrites in transverse section (Fig. 4b) and longitudinal section (Fig. 5d–f) of the DS specimens near the solid–liquid interface. Therefore, the α phase with hexagonal crystal structure is the primary phase of the Ti–46Al–0.5W–0.5Si (at%) alloy.

Because of the low solubility in the matrix, the element of Si is rejected from the solidified phase. The solubility of Si in the γ or α phase is less than 0.4 at% (Table 2). Therefore, the Ti_5Si_3 phase can be formed in the residual liquid phase during solidification. As shown in Fig. 6, Ti_5Si_3 phases distribute between grains and along the grains boundaries. The volume fraction of primary Ti_5Si_3 phase increases with the increase of growth rate in DS specimens. Because the specimen is growing with the planar interface at the lower growth rate, Si is enriched in the liquid phase before the solid–liquid interface and Ti_5Si_3 phases are formed in the last solidification region (Fig. 6e). Therefore, there are few Ti_5Si_3 phases in DS specimens at lower growth rates. At higher growth rates, the specimens grow with the cellular or dendritic interface, and Si is enriched in the residual liquid phase between cells or dendrites. Then, the Ti_5Si_3 phases are formed in these regions. Consequently, the volume fraction of Ti_5Si_3 phase increases with the increase of growth rate.

The B_2 phase can be formed in TiAl based alloys with the additional element W, such as in Ti–46Al–2W–0.5Si (at%) [17] and Ti–47Al–2W–0.5Si (at%) alloys [29,30], but the B_2 phase

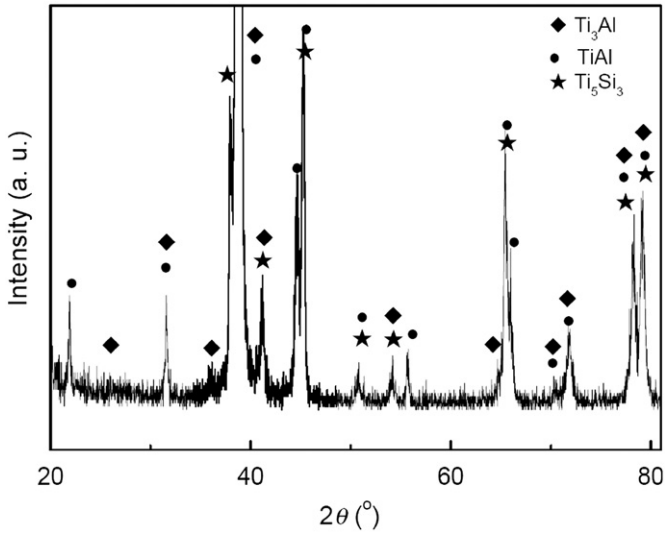

Fig. 3. XRD diffraction pattern of the directionally solidified Ti–46Al–0.5W–0.5Si (at%) alloy.

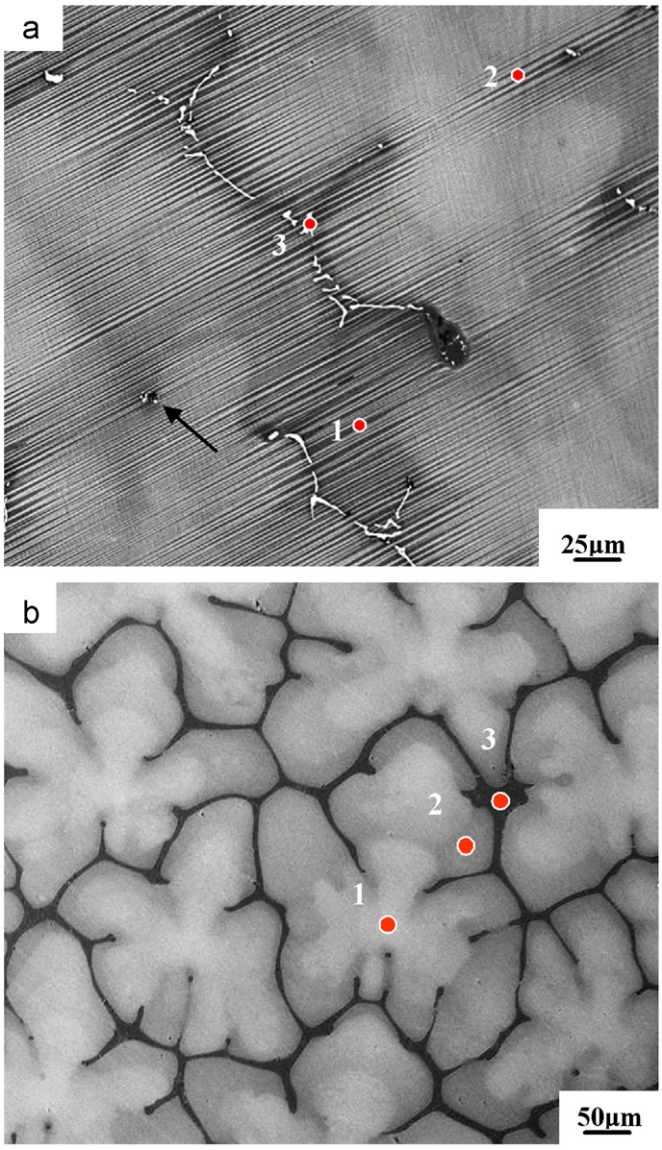

Fig. 4. BSE micrographs show the typical microstructure in the transverse section of the directional solidification ingot in directional solidification region (a) and quenched zone near the solid–liquid interface (b) at growth rate of 30 μm/s. The arrow indicates the Al_2O_3 particles.

Table 2
Chemical composition (at%) of the present phases in the Ti–46Al–0.5W–0.5Si (at%) alloy analyzed by EDS corresponding to Fig. 4a.

Phase	Ti	Al	W	Si
γ phase (point 1)	49.21	49.83	0.95	0.01
α_2 phase (point 2)	55.02	43.81	0.88	0.29
Ti_5Si_3 phase (point 3)	59.10	12.52	0.41	27.97

The B_2 phase can be formed in TiAl based alloys with the additional element W, such as in Ti–46Al–2W–0.5Si (at%) [17] and Ti–47Al–2W–0.5Si (at%) alloys [29,30], but the B_2 phase

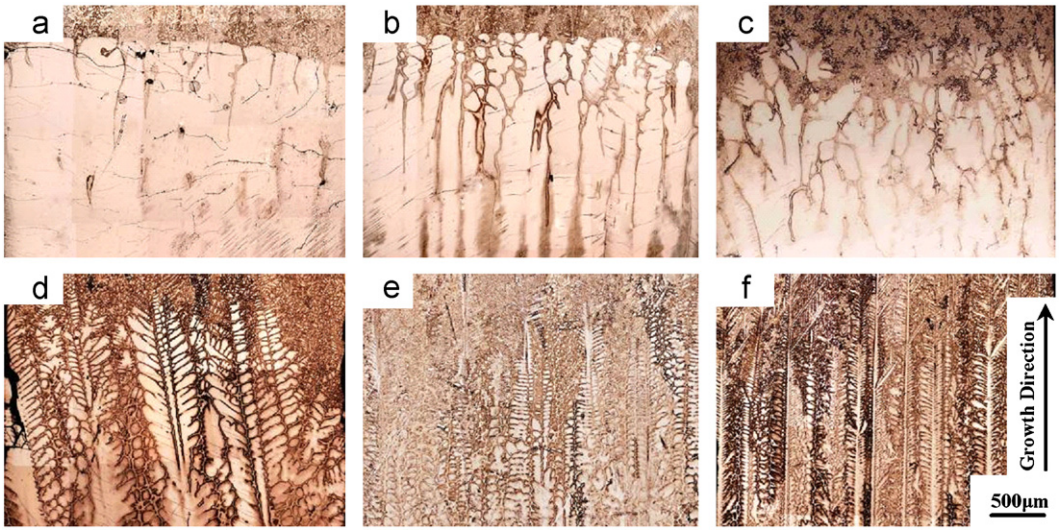

Fig. 5. Morphologies of solid–liquid interface of the directionally solidified Ti–46Al–0.5W–0.5Si (at%) alloy at different growth rates: nearly planar interface at the growth rate of 1 μm/s (a); cellular interface at the growth rate of 2 μm/s (b); cellular/dendritic interface at the growth rate of 3 μm/s (c); dendritic interface at growth rates of 15 μm/s (d), 30 μm/s (e) and 70 μm/s (f).

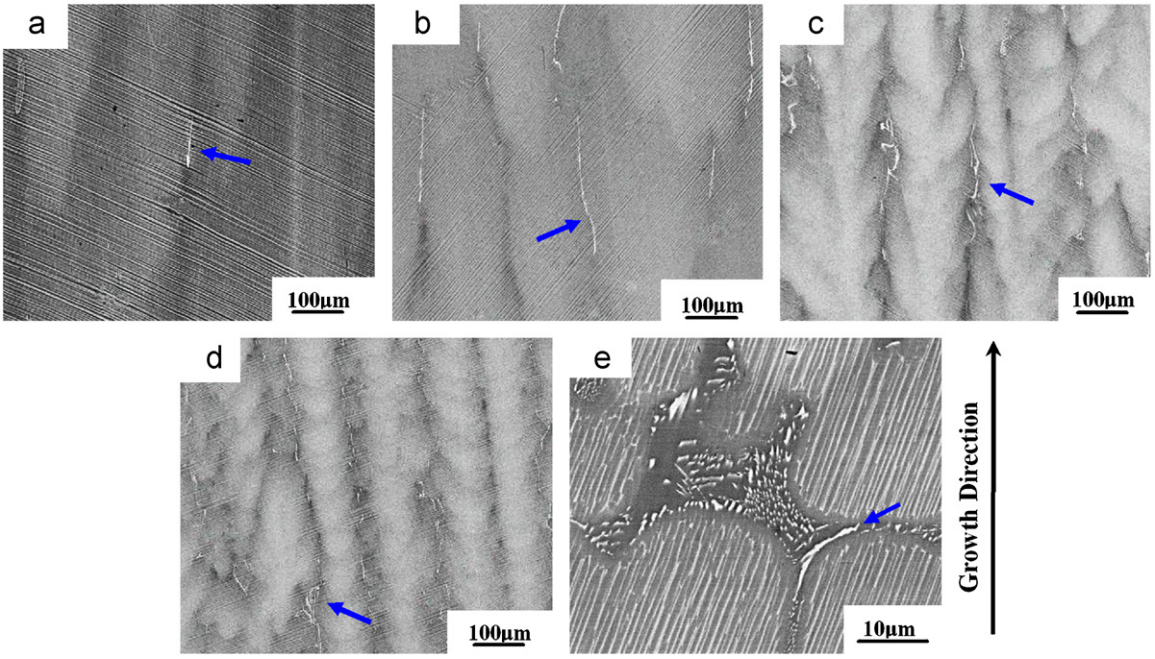

Fig. 6. BSE images of microstructure in longitudinal section of the specimens at different growth rates of 3 μm/s (a), 10 μm/s (b), 50 μm/s (c), 70 μm/s (d) and 1 μm/s (e). The enrichment of Si in front of the solid–liquid interface at the growth rate of 1 μm/s is shown in (e). The arrows indicate Ti_5Si_3 phases, which is the bright phase in these images.

Table 3
EDS results corresponding to the points in Fig. 4b (at%).

Position	Ti	Al	W	Si
Point 1	52.70	46.18	0.94	0.18
Point 2	49.82	48.83	0.83	0.52
Point 3	44.16	51.38	0.17	4.29

cannot be observed in the DS Ti–46Al–0.5W–0.5Si (at%) alloy in present experiments. Yin et al. [19] have indicated that the amount of B_2 phases reduced with the decrease of tungsten content. Therefore, B_2 phase is not formed in present alloy because of the lower content of W.

From the atomic contrast of the BSE image of the transverse section shown in Fig. 4b, the composition of the dendritic cores enriches in W and Ti compared with the interdendritic regions. The compositions analyzed by EDS for points labeled in Fig. 4b are listed in Table 3. The content of W in the dendritic core is 0.94 at%, which is higher than the value of 0.17 at% in the interdendritic region. Therefore, W segregates in α dendritic core.

3.2.2. *Solidification path*

Fig. 2 shows the formation of microstructure during solidification. First, the α phase is formed as a primary phase from the liquid. During the formation of α phase, the element of Si is rejected from the solidified phase and enriches in the residual

Table 4
Solidified structure, lamellar orientation and PGD of α phase for different solidification conditions.

Growth rate (μm/s)	Interface morphology	Mainly lamellar orientation (deg.)	PGD of α phase
1	Nearly planar	88	⟨0001⟩
2	Cellular	85	⟨0001⟩
3	Cellular/dendritic	65	⟨10$\bar{1}$1⟩
5	Cellular/dendritic	90	⟨0001⟩
8	Cellular/dendritic	70	⟨10$\bar{1}$1⟩
10	Dendritic	50	⟨10$\bar{1}$1⟩
15	Dendritic	62	⟨10$\bar{1}$1⟩
20	Dendritic	77	⟨$\bar{2}\bar{2}$43⟩
25	Dendritic	78	⟨$\bar{2}\bar{2}$43⟩
30	Dendritic	47	⟨$\bar{2}\bar{2}$43⟩
40	Dendritic	74	⟨$\bar{2}\bar{2}$43⟩
50	Dendritic	56	⟨10$\bar{2}$1⟩
60	Dendritic	47	⟨$\bar{2}\bar{2}$43⟩
70	Dendritic	79	⟨$\bar{2}\bar{2}$43⟩
80	Dendritic	69	⟨10$\bar{1}$1⟩
90	Dendritic	68	⟨10$\bar{1}$1⟩
100	Dendritic	71	⟨10$\bar{1}$1⟩

liquid phase (L_1) between dendrites. Second, with the solidification continuing, Ti_5Si_3 phases are formed between dendrites. Before the temperature reaches the temperature of eutectoid reaction, there is α single-phase field in the specimen. Then, the α phase changes into α_2/γ lamellar structure. The solid phase transition interface can be preserved by quenching, as shown in Fig. 2a3. The solid phase transition interface has an irregular shape in the specimens with the dendritic solid–liquid interface (Fig. 2b3 and c3). The white phases in mushy zone are residual α phases, which are surrounded by γ/α_2 lamellar structures. Lastly, the DS specimen is composed of α_2/γ lamellar structures and fine Ti_5Si_3 precipitates.

Therefore, the solidification path of the alloy is proposed to be $L \rightarrow L_1+\alpha \rightarrow T_{i5}Si_3+\alpha \rightarrow Ti_5Si_3+[\alpha_2+\gamma]$.

3.3. Morphologies of solid–liquid interface and dendritic structure

Morphologies of the solid–liquid interface can be classified into three types, which are cellular, cellular/dendritic and dendritic interfaces (Fig. 5). Table 4 shows the variation of the solid–liquid interface morphology with growth rates. Nearly planar interface is observed at the growth rate of 1 μm/s (Fig. 5a). As the growth rate increases to 2 μm/s, the nearly planar interface transforms to cellular (Fig. 5b). A transition structure composed of cells and dendrites is found at the growth rate of 3 μm/s (Fig. 5c). Some cells have the tendency to form secondary dendritic arms. The regular dendritic interface is formed when the growth rates are above 10 μm/s (Fig. 5d–f). The dendritic arrays are well aligned along the growth direction when the growth rates are above 15 μm/s.

The criterion for the stability of the planar solid–liquid interface in multi-component alloys can be simplified as [31,32]

$$\frac{G_{eff}}{V} \geq \frac{\Delta T_0}{D_L} \quad (1)$$

where G_{eff} is the effective temperature gradient at the solid–liquid interface, ΔT_0 is the melting range of the alloy and D_L is the solute diffusion coefficient of Al in the liquid. According to Ref. [32], the effective temperature gradient G_{eff} can be replaced by G_L, when the Peclet number (Pe) is small ($Pe<0.1$). The diffusion coefficient in the liquid is assumed as $D_L=2.8\times10^{-9}$ mm^2/s [33]. The melting range $\Delta T=T_L-T_S$ is determined by DTA analysis from the measurements of the solidus temperature ($T_s=1701$ K) and liquidus temperature ($T_L=1767$ K). The measured melting range

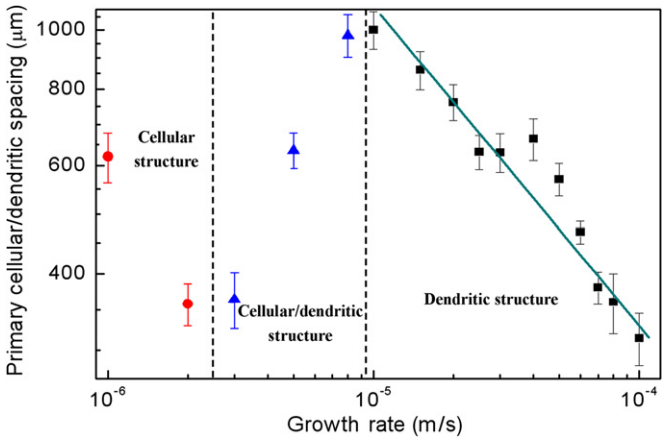

Fig. 7. Variation of the primary cellular or dendritic spacing as a function of the growth rate.

of present alloy is 66 K. The critical value (G_L/V) for planar front solidification is calculated to be 2.4×10^{10} Ks/m^2. Hence, the critical growth rate of transition from the planar to cellular solid–liquid interface is about $V_c=0.8$ μm/s. However, such a low growth rate obviously increases the reaction time between the melt and the mold. The volume fraction of Al_2O_3 particles will increase, which will influence the microstructure formation of the DS specimens [17,34].

The primary cellular or dendritic spacing alters with the growth rate (Fig. 7). For cells, the spacing decreases with the increase of growth rate. The lowest value in the cellular spacing is at the growth rate of 2 μm/s. In the cellular/dendritic region, the primary spacing (λ_1) increases with the increasing growth rate. In the dendritic region, the values of λ_1 decrease with the increase of growth rate. For regular dendrites, λ_1 decreases proportionally with the increasing growth rate according to the relationship:

$$\lambda_1 = K_1 V^{-m}, \quad (2)$$

where K_1 is a material constant and m is the rate exponent. Using linear regression analysis, the experimental data can be expressed as

$$\lambda_1 = 3.63\times10^{-6}V^{-0.47} \quad (3)$$

The regression coefficient of this fit is $r^2=0.96$. The exponent value 0.47 is close to the theoretical value of 0.5 resulting from models of Okamoto–Kishitake [35] and Bouchard–Kirkaldy [36]. The exponent value is smaller than the theoretical value of 0.59 resulting from the model of Hunt–Lu [37]. However, the exponent value is greater than the theoretical value of 0.25 from the models of Hunt [38], Kurz–Fisher [39], Kurz–Fisher [23] and Trivedi Model [40]. The difference might be due to the theoretical models developed for dilute and binary alloy. The models of Hunt [38] and Trivedi [40] considered the flux balance for a small inter-dendritic volume element, which is not suitable for multi-component alloys. It suggests that some theoretical models need to be modified to describe the primary spacing of multi-component alloys.

The exponent value of λ_1 agrees well with 0.44 obtained by Fan et al. [41] for the Ti–43Al–3Si (at%) alloy. However, the exponent value is greater than 0.24 obtained by Lapin et al. [17] for the Ti–46Al–2W–0.5Si (at%) alloy, and 0.30 obtained by Fan et al. [42] for the Ti–49Al (at%). Differences of these values could be due to the different composition of alloys and solidification conditions. The exponent value could be dependent on the component of alloys.

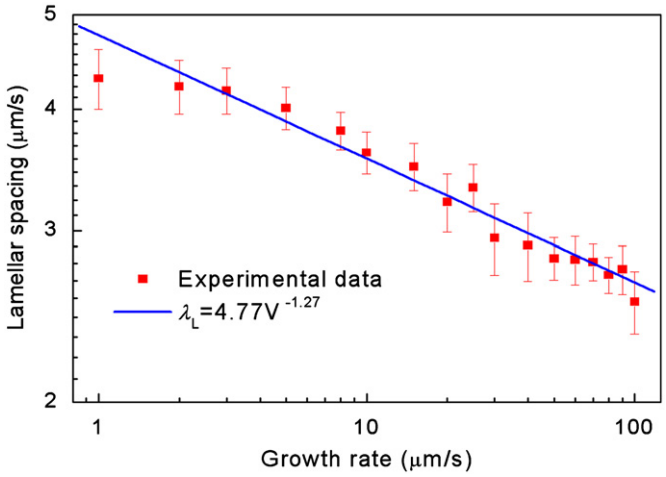

Fig. 8. Dependence of the interlamellar spacing on the growth rate.

3.4. Lamellar structure

3.4.1. Interlamellar spacing

The interlamellar spacing decreases with the increasing growth rate (Fig. 8). The dependence of interlamellar spacing on the growth rate is given as follows:

$$\lambda_L = K_2 V^{-n} \tag{4}$$

where K_2 is a material constant and n is the rate exponent. Using linear regression analysis, the experimental data can be expressed as follows:

$$\lambda_L = 4.77V^{-0.127} \tag{5}$$

The regression coefficient of this fit is $r^2=0.98$. The rate exponent $n=0.127$ is smaller than the value 0.46 obtained by Lapin et al. [17] for the Ti–46Al–2W–0.5Si (at%) alloy, 0.44 obtained by Fan et al. [41] for the Ti–43Al–3Si (at%) alloy and 0.41 obtained by Fan et al. [42] for the Ti–49Al (at%). Differences in these values might be due to the different composition of alloys and the different temperature gradient in directional solidification experiments.

3.4.2. Orientation of lamellar structure

The primary phase of TiAl alloys determines the final lamellar orientation because of the crystallographic orientation relationship among β, α and γ phase, namely $\{110\}_\beta//(0001)_\alpha//\{111\}_\gamma$ and $\langle 111\rangle_\beta//\langle 11\bar{2}0\rangle_\alpha//\langle 110\rangle_\gamma$ [5,8–10]. If the β phase is the primary phase, the preferred growth direction (PGD) of β phase is $\langle 001\rangle$ direction, and then the lamellar orientation is 0° or 45° inclined to growth direction. If the α phase is the primary phase, the PGD of α phase is $\langle 0001\rangle$ direction, and then the lamellar orientation is 90° inclined to growth direction. However, lamellar orientations are not perpendicular to the growth direction in present experiments, even if the α phase is the primary phase. The lamellar structures are oriented about 45–90° to the growth direction (Table 4). This phenomenon can be attributed to the variation of PGD of the α phase under different solidification conditions.

On one hand, the lamellar structures in directional solidification region have the same orientation as that of the unmelted region (Fig. 2). The unmelted region has the effect of the seeding material at the beginning of directional solidification. The lamellar structure in directional solidification region obtains the lamellar orientation of unmelted region and restores it during solidification. The lamellar orientation in directional solidification region is history-dependent on that of unmelted as-cast crystals near the initial interface of directional solidification. Thus, the preferred growth direction (PGD) of α phase is not $\langle 0001\rangle$ direction and the orientation of lamellar is not perpendicular to the growth direction. These as-cast crystals may act as a seed to control the lamellar orientation of subsequent crystals in directional solidification. The alloy can act as a seeding material to grow ingots with similar composition and to control the lamellar orientation parallel to the growth direction.

On the other hand, the changing of the PGD of α phase affects the lamellar orientation. The lamellar orientation is not just 0° or 45° inclined to growth direction in β solidification TiAl alloys. In Ti–47.5Al–2W–0.5Si (at%) and Ti–46Al–2Mo–2Nb (at%) alloys [43], the lamellar orientation is angled or normal to the growth direction near the top of the directionally solidified specimens. Jung et al. [44] have indicated that the lamellar orientation in the DS Ti–47Al–2W (at%) alloy inclined at angles of 60–90° to growth direction at the growth rate of 90 mm/h. Xiao et al. [45] have found that the lamellar orientation was not angled 0° or 45° to the growth direction, and other orientations (e.g. 74°, 80° and 84°) also formed in the DS Ti–47Al–2Cr–2Nb (at%) alloy. Jung et al. [44] and Xiao et al. [45,46] have considered that the departure of lamellar orientation resulted from the changed growth direction of β phase.

For the present alloy, which is α solidification, the lamellar orientation is not perpendicular to the growth direction under different growth rates can also be explained in this way. The PGD of α phase is shown in Table 4, which was calculated according to the method in Refs. [44–46]. The PGD of α phase is $\langle 10\bar{1}1\rangle$ or $\langle 0001\rangle$ direction at low growth rates (between 1 μm/s and 15 μm/s). When growth rates are between 20 and 70 μm/s, the PGD of α phase is $\langle \bar{2}\bar{2}43\rangle$ direction. The PGD of α phase changes into $\langle 10\bar{1}1\rangle$ direction at higher growth rate (between 80 and 100 μm/s). With increasing growth rate, the PGD of α phase changes from $\langle 0001\rangle$ to $\langle 10\bar{1}1\rangle$, and then to $\langle \bar{2}\bar{2}43\rangle$, and to $\langle 10\bar{1}1\rangle$ at higher growth rates.

The variation of the PGD of α phase is caused by the changing of solid–liquid interface morphologies with the increase of the growth rate. The α phase does not grow along $\langle 0001\rangle$ direction under the effect of heat flow and crystallographic orientation. The driving forces determining the PGD of phase are interface kinetics and anisotropic energy [47]. However, Haxhimali et al. [48] have indicated that Al has weak solid–liquid interface energy anisotropy, and the solute effects can induce greater varieties of interface energy anisotropy of Al–Zn alloy. Therefore, for TiAl alloys, the variation of heat flow and growth rate in directional solidification can cause the change of interface energy anisotropy of the α phase, and conduce the changing of PGD. Since the lamellar orientation obeys the relationship of $(0001)_\alpha//\{111\}_\gamma$ and $\langle 11\bar{2}0\rangle_\alpha//\langle 110\rangle_\gamma$, the lamellar orientation is not perpendicular to the growth direction if the PGD is not in $\langle 0001\rangle$ direction.

4. Conclusions

(1) For the Ti–46Al–0.5W–0.5Si (at%) alloy, the morphology of solid/liquid interface transforms from nearly planar to cellular and then to dendritic with the increasing growth rate. The hexagonal α phase is the primary phase in the studied alloy. The solidification path of the alloy is: $L\rightarrow L+\alpha\rightarrow Ti_5Si_3+\alpha\rightarrow Ti_5Si_3+[\alpha_2+\gamma]$.

(2) Tungsten segregates in dendritic cores of α phase and Si enriches in interdendritic regions. The enrichment of Si in interdendritic regions leads to the Ti_5Si_3 phase. The Ti_5Si_3 phase distributes in grain boundaries.

(3) For cells, the spacing decreases with the increasing growth rate. In cellular/dendritic region, the primary spacing increases with the increasing growth rate. The primary dendrite arm

spacing decreases with the increase of growth rate according to relationship: $\lambda_1 \propto V^{-0.47}$.

(4) The interlamellar spacing decreases with the increase of growth rate according to relationship: $\lambda_L \propto V^{-0.127}$.

(5) Though α phase is the primary phase, the lamellar orientation is not perpendicular to the growth direction. The variation of lamellar orientation can be attributed to two factors. One is the history-dependence on the lamellar orientation of unmelted as-cast crystals near the initial interface of directional solidification. The other is the variation of the preferred growth directions of α phase.

Acknowledgments

The authors are grateful to the financial support of the National Natural Science Foundation of China (Grant nos. 50801019, 51071062 and 50771041) State Key Lab of Advanced Metals Materials (Grant no. 2009ZD-06) and Project 973 (Grant no. 2011CB610406).

Appendix A. Growth direction calculation of α phase

The details for calculating the preferred growth direction of α phase are illustrated as follows:

(1) The angle (η) between the $\{111\}_\gamma$ plane of γ lamellae and the growth direction is measured from optical microscopy images. The angle (θ) between $\langle 111\rangle_\gamma$ crystal index and growth direction is obtained from $\theta = 90^\circ - \eta$. The crystal index $\langle uvw\rangle_\gamma$ along the growth direction is calculated using the following equation [49]:

$$\cos\Theta = \frac{u_1u_2 + v_1v_2 + w_1w_2}{\sqrt{(u_1^2+v_1^2+w_1^2)(u_2^2+v_2^2+w_2^2)}} \tag{A1}$$

where $\langle u_1v_1w_1\rangle_\gamma$ and $\langle u_2v_2w_2\rangle_\gamma$ present different crystal indices of γ phase, and Θ is the angle between the two directions. In this study, $\langle u_1v_1w_1\rangle$ is $\langle 111\rangle_\gamma$ and Θ is θ. Then $\langle u_2v_2w_2\rangle_\gamma$, namely $\langle uvw\rangle_\gamma$ is the possible direction need to be calculated.

(2) All possible angles between $\langle uvw\rangle_\gamma$ and the reference crystal index $\langle 111\rangle_\gamma$ (or $\langle 110\rangle_\gamma$) are calculated by Eq. (A1), and denoted by angle group $\{\delta_1\}$ (or $\{\delta_2\}$).

(3) Assuming that $\langle HKTL\rangle_\alpha$ is the growth direction of α dendrites. The values of φ_1 and φ_2 stand for the angles between $\langle HKTL\rangle_\alpha$ and $\langle 0001\rangle_\alpha$, and $\langle HKTL\rangle_\alpha$ and $\langle 11\bar{2}0\rangle_\alpha$, respectively. When calculating, the four-index $\langle HKTL\rangle_\alpha$ need to be converted to three-index $\langle hkl\rangle_\alpha$. The values of φ are calculated using the following equation [49]:

$$\cos\Phi = \frac{h_1h_2 + k_1k_2 - 1/2(h_1k_2 + h_2k_1) + l_1l_2}{\sqrt{h_1^2+k_1^2-h_1k_1+(c/a)^2l_1^2}\sqrt{h_2^2+k_2^2-h_2k_2+(c/a)^2l_2^2}} \tag{A2}$$

(4) The angle δ_1' (or δ_2'), which is selected from the angle group $\{\delta_1\}$ (or $\{\delta_2\}$), is the closest to φ_1 (or φ_2). If the error Δ, $|\delta_1 - \varphi_1'|$ (or $|\delta_2 - \varphi_2'|$), is less than the angle (ψ) between the dendritic growth direction and the withdrawal direction, it can be confirmed that $\varphi_1 = \delta_1'$ and $\varphi_2 = \delta_2'$ ($\varphi < 9^\circ$). Therefore, the $\langle HKTL\rangle_\alpha$ is the preferred growth direction of α dendrites.

References

[1] X. Wu, Review of alloy and process development of TiAl alloys, Intermetallics 14 (2006) 1114–1122.
[2] H. Clemens, H. Kestler, Processing and applications of intermetallic γ-TiAl-based alloys, Advanced Engineering Materials 2 (2000) 551–570.
[3] D.M. Dimiduk, Gamma titanium aluminide alloys—an assessment within the competition of aerospace structural materials, Materials Science and Engineering: A 263 (1999) 281–288.
[4] Y.W. Kim, Ordered intermetallic alloys, part III: gamma titanium aluminide, JOM (1994) 30–39.
[5] D.R. Johnson, H. Inui, M. Yamaguchi, Directional solidification and microstructural control of the TiAl/Ti_3Al lamellar microstructure in TiAl–Si alloys, Acta Materialia 44 (1996) 2523–2535.
[6] W. Luo, J. Shen, Z. Min, H. Fu, Lamellar orientation control of TiAl alloys under high temperature gradient with Ti–43Al–3Si seed, Journal of Crystal Growth 310 (2008) 5441–5446.
[7] S.E. Kim, Y.T. Lee, M.H. Oh, H. Inui, M. Yamaguchi, Directional solidification of TiAl–Si alloys using a polycrystalline seed, Intermetallics 8 (2000) 399–405.
[8] D.R. Johnson, H. Inui, S. Muto, Y. Omiya, T. Yamanaka, Microstructural development during directional solidification of α-seed TiAl alloys, Acta Materialia 54 (2006) 1077–1085.
[9] T. Yamanaka, D.R. Johnson, H. Inui, M. Yamaguchi, Directional solidification of TiAl–Re–Si alloys with aligned γ/α_2 lamellar microstructures, Intermetallics 7 (1999) 779–784.
[10] H. Fu, J. Guo, Y. Su, D. Xu, J. Li, Directional solidification and lamellar orientation control of TiAl intermetallics, Chinese Journal of Nonferrous Metals 13 (2003) 797–910.
[11] H.N. Lee, D.R. Johnson, H. Inui, M.H. Oh, D.M. Wee, M. Yamaguchi, Microstructure control though seeding and directional solidification of TiAl alloys containing Mo and C, Acta Materialia 48 (2000) 3221–3233.
[12] D.R. Johnson, Y. Masuda, H. Inui, M. Yamaguchi, Alignment of the TiAl/Ti_3Al lamellar microstructure in TiAl alloys by directional solidification, Materials Science and Engineering: A 239–240 (1997) 577–583.
[13] M. Yamaguchi, D.R. Johnson, H.N. Lee, H. Inui, Directional solidification of TiAl-based alloys, Intermetallics 8 (2000) 511–517.
[14] H.N. Lee, D.R. Johnson, H. Inui, M.H. Oh, D.M. Wee, M. Yamaguchi, A composition window in the TiAl–Mo–Si system suitable for lamellar structure control through seeding and directional solidification, Materials Science and Engineering: A 329–331 (2002) 19–24.
[15] D.R. Johnson, H. Inui, M. Yamaguchi, Directional solidification and microstructural control of the TiAl/Ti_3Al lamellar microstructure in TiAl–Si alloys, Acta Materialia 44 (1996) 2523–2535.
[16] S.W. Kim, K.S. Kumar, M.H. Oh, D.M. Wee, Crack propagation behavior in TiAl–Nb single and Bi-PST crystals, Intermetallics 15 (2007) 976–984.
[17] J. Lapin, L. Ondrúš, M. Nazmy, Directional solidification of intermetallic Ti–46Al–2W–0.5Si alloy in alumina moulds, Intermetallics 10 (2002) 1019–1031.
[18] G.E. Fuchs, Effect of W additions to Ti–48Al–2Nb–2Cr alloys, Materials Science and Engineering: A 192–193 (1995) 707–715.
[19] W.M. Yin, V. Lupinc, L. Battezzati, Microstructure study of a γ-TiAl based alloy containing W and Si, Materials Science and Engineering: A 239–240 (1997) 713–721.
[20] B.G. Kim, G.M. Kim, C.J. Kim, Oxidation behavior of TiAl–X (X=Cr, V, Si, Mo or Nb) intermetallics at elevated temperature, Scripta Materialia 33 (1995) 1117–1125.
[21] W.M. Yin, V. Lupinc, Silicide precipitation in a γ-based Ti–47Al–2W–0.5Si alloy, Scripta Materialia 37 (1997) 211–217.
[22] U. Hecht, L. Grńsy, T. Pusztai, B. Böttger, M. Apel, V. Witusiewicz, L. Ratke, J. De Wilde, L. Froyen, D. Camel, B. Drevet, G. Gaivre, S.G. Fries, B. Legendre, S. Rex, Multiphase solidification in multicomponent alloys, Materials and Science Engineering: R 46 (2004) 1–49.
[23] W. Kurz, D.J. Fisher, Fundamentals of Solidification, Trans Tech Publications, Aedermannsdorf, Switzerland, 1989 (p. 86).
[24] D.R. Johnson, Y. Masuda, H. Inui, M. Yamaguchi, Alignment of the TiAl/Ti_3Al lamellar microstructure in TiAl alloys by growth from a seed material, Acta Materialia 45 (1997) 2523–2533.
[25] L.S. Luo, Y.Q. Su, J.J. Guo, X.Z. Li, S.M. Li, H. Zhong, L. Liu, H.Z. Fu, Peritectic reaction and its influences on the microstructures evolution during directional solidification of Fe–Ni alloys, Journal of Alloys and Compounds 461 (2008) 121–127.
[26] H. Kaya, M. Gündüz, E. Çadırlı, N. Maraşlı, Dependency of microindentation hardness on solidification processing parameters and cellular spacing in the directionally solidified Al based alloys, Journal of Alloys and Compounds 478 (2009) 281–286.
[27] U. Böyük, N. Maraşlı, The microstructure parameters and microhardness of directionally solidified Sn–Ag–Cu eutectic alloy, Journal of Alloys and Compounds 485 (2009) 264–269.
[28] E. Çadırlı, H. Kaya, M. Gündüz, Effect of growth rates and temperature gradients on the lamellar spacing and undercooling in the directionally solidified Pb–Cd eutectic alloy, Materials Research Bulletin 38 (2003) 1457–1476.
[29] R. Yu, L.L. He, Z.X. Jin, J.T. Guo, H.Q. Ye, V. Lupinc, On the orientation relationship between Ti_5Si_3 precipitates and B_2 phase in a Ti–47Al–2W–0.5Si alloy, Scripta Materialia 44 (2001) 911–916.
[30] R. Yu, L.L. He, J.T. Guo, H.Q. Ye, V. Lupinc, Orientation relationship and interfacial structure between ξ-Ti_5Si_3 precipitates and γ-TiAl intermetallics, Acta Materialia 48 (2000) 3701–3710.
[31] R. Trivedi, W. Kurz, Modeling of solidification microstructure inconcentrated solutions and intermetallic systems, Metallurgical Transactions A 21 (1990) 1311–1318.

[32] J. Lapin, A. Klimová, R. Velísek, M. Kursa, Directional solidification of Ni–Al–Cr–Fe alloy, Scripta Materialia 37 (1997) 85–91.
[33] Y. Liu, G. Yang, Y. Zhou, High-velocity banding structure in the laser-resolidified hypoperitectic $Ti_{47}Al_{52}$ alloy, Journal of Crystal Growth 240 (2002) 603–610.
[34] J. Lapin, L. Ondrúš, O. Bajana, Effect of Al_2O_3 particles on mechanical properties of directionally solidified intermetallic Ti–46Al–2W–0.5Si alloy, Materials Science and Engineering: A 360 (2003) 85–95.
[35] T. Okamoto, K. Kishitake, Dendritic structure in unidirectionally solidified aluminum, tin, and zinc base binary alloys, Journal of Crystal Growth 29 (1975) 137–146.
[36] D. Bouchard, J.S. Kirkaldy, Prediction of dendrite arm spacings in unsteady- and steady-state heat flow of unidirectionally solidified binary alloys, Metallurgical and Materials Transactions B 28 (1997) 633–651.
[37] J.D. Hunt, S.Z. Lu, Numerical modeling of cellular/dendritic array growth: spacing and structure predictions, Metallurgical and Materials Transactions A 27 (1996) 611–623.
[38] J.D. Hunt, Solidification and Casting of Metals, The Metals of Society, London, 1979 (p. 9).
[39] W. Kurz, D.J. Fisher, Dendritic growth at the limit of stability: tip radius and spacing, Acta Materialia 29 (1981) 11–20.
[40] R. Trivedi, Interdendritic spacing: part II. A comparison of theory and experiment, Metallurgical and Materials Transactions A 15 (1984) 977–982.
[41] J. Fan, X. Li, Y. Su, J. Guo, H. Fu, The microstructure parameters and microhardness of directionally solidified Ti–43Al–3Si alloy, Journal of Alloys and Compounds 506 (2010) 593–599.
[42] J. Fan, X. Li, Y. Su, J. Guo, H. Fu, Effect of growth rate on microstructure parameters and microhardness in directionally solidified Ti–49Al alloy, Materials and Design (2011). doi:10.1016/j.matdes.2011.05.007.
[43] H. Saari, J. Beddoes, D.Y. Seo, L. Zhao, Development of directionally solidified γ-TiAl structures, Intermetallics 13 (2005) 937–943.
[44] I.S. Jung, M.H. Oh, N.J. Park, S. Kumar, D.M. Wee, Lamellar boundary alignment of DS-processed TiAl–W alloys by a solidification procedure, Metals and Materials International 13 (2007) 455–462.
[45] Z. Xiao, L. Zheng, L. Yang, J. Yan, H. Zhang, Effects of temperature gradient on lamellar orientations of directionally solidified TiAl-based alloy, Acta Metallurgica Sinica 46 (2010) 1229–1233.
[46] Z. Xiao, L. Zheng, J. Yan, L. Yang, H. Zhang, Lamellar orientation and growth directions of β dendritic in directionally solidified Ti–47Al–2Cr–2Nb alloy, Journal of Crystal Growth 324 (2011) 309–313.
[47] M.C. Flemings, Solidification Processing, McGraw-Hill, New York, 1974 (p. 159).
[48] T. Haxhimali, A. Karma, F. Gonzales, M. Rappaz, Orientation selection in dendritic evolution, Nature Materials 5 (2006) 660–664.
[49] J. Pan, J. Tong, M. Tian, Foundation of Materials Science, Tsinghua University Press, Beijing, 1998 (p. 40).